BNL-222409-2021-JAAM

Mechanistic Investigation of a Visible Light Mediated Dehalogenation/Cyclisation Reaction using Iron(III), Iridium(III) and Ruthenium(II) Photosensitizers

A. Aydogan, R. N. Sampaio

To be published in "Catalysis Science & Technology"

November 2021

Chemistry Department

Brookhaven National Laboratory

U.S. Department of Energy

USDOE Office of Science (SC), Basic Energy Sciences (BES) (SC-22)

DISCLAIMER

ARTICLE

Mechanistic Investigation of a Visible Light Mediated Dehalogenation/Cyclisation Reaction using Iron(III), Iridium(III) and Ruthenium(II) Photosensitizers

Received 00th January 20xx,
Accepted 00th January 20xx

DOI: 10.1039/x0xx00000x

Akin Aydogan,[a] Rachel E. Bangle,[b] Simon De Kreijger,[a] John C. Dickenson,[b] Michael L. Singleton,[a] Emilie Cauët,[c] Alejandro Cadranel,[d] Gerald J. Meyer,[b] Benjamin Elias,[a] Renato N. Sampaio*[b,e] and Ludovic Troian-Gautier,*[a]

The mechanism of a visible light-driven dehalogenation/cyclization reaction was investigated using ruthenium(II), iridium(III) and iron(III) photosensitizers by means of steady-state photoluminescence, time-resolved infrared spectroscopy, and nanosecond/femtosecond transient absorption spectroscopy. The nature of the photosensitizer was found to influence the products distribution such that the dehalogenated, non-cyclized products were only detected for the iron photosensitizer. Strikingly, with the iron photosensitizer, large catalytic yields required a low dielectric solvent such as dichloromethane, consistent with a previous publication. This low dielectric solvent allowed ultrafast charge-separation to outcompete geminate charge recombination and improved cage escape efficiency. Further, the identification of reaction mechanisms unique to the iron, ruthenium, and iridium photosensitizer represents progress towards the long-sought goal of utilizing earth-abundant, first-row transition metals for emerging energy and environmental applications.

Introduction

Photochemically active, earth-abundant metal complexes are highly desirable, yet they have had limited success in comparison to well-studied 2nd and 3rd row transition metal complexes. Intense metal-to-ligand or ligand-to-metal charge transfer transitions in 1st row transition metal complexes result in visible light absorption comparable to that in 2nd and 3rd row complexes. However, fundamental electronic structural disparities between 3d and 4d/5d valence electrons generally result in 1st row transition metal complexes with short-lived excited states that do not undergo efficient diffusional reactivity.[1] In contrast, ruthenium, iridium, rhodium and osmium complexes with long-lived charge transfer excited states are champions for a variety of photochemical applications. The scarcity and high cost of 2nd and 3rd row transition metals, though, necessitates development of earth-abundant 1st row metal complexes with longer lived excited states.[2, 3] In recent years, numerous complexes based on copper,[4, 5] molybdenum,[6] nickel,[7, 8] tungsten,[9, 10] zirconium,[11, 12] chromium,[13-15] cobalt,[16] and manganese,[17] have been identified as promising candidates for photochemical applications. Iron's low cost, non-toxicity, and high abundance in earth's crust, however, has made iron complexes[1, 18-33] the 'holy grail' of green photochemistry.

Unlike ruthenium(II) counterparts, prototypical Fe(II) complexes such as $[Fe(bpy)_3]^{2+}$, where bpy is 2,2'-bipyridine, exhibit Metal-to-Ligand Charge Transfer (MLCT) excited-states that are rapidly deactivated by relaxation to a high-spin ^{5}MC (Metal Centered, $^5T_{2g}$) state.[1, 2] This non-luminescent excited state persists for 650 ps before relaxing back to the $^1A_{1g}$ ground state.[34-36] Stabilization of the MLCT state relative to the MC state would prevent or limit this deleterious deactivation pathway.[2] Through judicious design of ligand coordination environments that tune the electronic properties of Fe(II)-based photosensitizers, excited-state lifetimes have significantly increased, with examples of ~10 ps (2013),[25] ~26 ps (2016),[37] 100ps[32] (2017), 528 ps (2018),[38] and ~2.5 ns (2019).[33] Recently, a luminescent Fe(III) photosensitizer (**Figure 1**) exhibiting an unconventional low-lying ligand-to-metal charge transfer (^{2}LMCT) excited state was reported to have a ~2.2 ns lifetime in CH_3CN that was not quenched by oxygen in air.[27] Importantly, this photosensitizer was demonstrated to undergo light-driven bimolecular electron transfer reactions similar to ruthenium and osmium excited states.

The mechanism(s) of Fe(II/III) photoredox catalytic transformations are often ill-defined or simply unknown. For example, salts such as $FeSO_4$ and $FeBr_3$ have been proposed to form *in situ* photosensitizers and initiate some of the observed

[a] Université catholique de Louvain (UCLouvain), Institut de la Matière Condensée et des Nanosciences (IMCN), Molecular Chemistry, Materials and Catalysis (MOST), Place Louis Pasteur 1, bte L4.01.02, 1348 Louvain-la-Neuve, Belgium
[b] Department of Chemistry, University of North Carolina at Chapel Hill, Chapel Hill, North Carolina, 27599-3290, United States
[c] Spectroscopy, Quantum Chemistry and Atmospheric Remote Sensing (CP 160/09), Université libre de Bruxelles, 50 av. F. D. Roosevelt, B-1050 Brussels, Belgium
[d] Department of Chemistry and Pharmacy, Interdisciplinary Center for Molecular Materials (ICMM), Friedrich-Alexander-Universität Erlangen-Nürnberg, Egerlandstr. 3, 91058 Erlangen, Germany
[e] Chemistry Division, Brookhaven National Laboratory, Upton, NY 11973-5000, USA
* Corresponding Authors. Ludovic.troian@uclouvain.be, renatons@email.unc.edu
Electronic Supplementary Information (ESI) available: NMR Characterization, excited-state quenching experiments, steady-state illuminations and additional photoredox transformations. See DOI: 10.1039/x0xx00000x

chemical transformations such as intramolecular aromatic C–H acyloxylation,[39] aerobic oxidative transposition of a benzylic C(sp^3–H) bond,[40] and the aminoselenation of alkenes.[41] More well-defined photosensitizers, such as $[Fe(bpy)_3]^{2+}$ and $[Fe(phen)_3]^{2+}$, where phen is 1,10-phenanthroline, have been reported to catalyze the enantioselective alkylation of aldehydes[42] and the photochemical synthesis of carbazole, but mechanisms have not been formally investigated.[43] The scope of Fe photocatalysis has historically been limited, as low-lying MC states in Fe(II) photosensitizers act as an energy sink compared to the ~2 eV typically stored in Ru(II) and Ir(III) MLCT excited states. The assumption that these MC states are unproductive, however, has recently been questioned by McCusker *et al.*[18] who reported a low-spin diamagnetic $[Fe^{II}(tren(py)_3)]^{2+}$ complex (where $tren(py)_3$ = tris(2-pyridyl-methylimino-ethyl)amine), which produces a high spin MC state ($^5T_2$) that persists for 55 ns. This newly identified MC excited state was shown to initiate diffusional bimolecular electron transfer with a series of quinone electron acceptors.[18]

The range of Fe-based photosensitizers that drive the catalytic transformation of organic substrates continues to expand. The authors recently showed that the LMCT excited state of $[Fe(phtmeimb)_2]^+$, where phtmeimb = phenyltris(3-methyl-imidazolin-2-ylidene)borate, originally reported by Wämmark *et al.*,[27] was able to perform the visible light-mediated dehalogenation of an organic substrate.[44] A systematic analysis of spectroscopic data with UV-visible and infrared spectroscopy provided a detailed mechanistic picture of the photoredox transformations. The important utilization of time-resolved infrared spectroscopy provided critical insights into the kinetics for the formation and reactivity of radical intermediates that were used to construct a detailed catalytic cycle. It was also noted that choice of solvent had a dramatic impact on the cage escape yield of electron transfer products, but the physical origins of this behavior remain speculative. Nevertheless, the solvent influence on the cage escape yield was vital to the overall reaction yield with $[Fe(phtmeimb)_2]^+$ and may be generalizable to other Fe photosensitizers acting through similar mechanisms. Hence, fundamental studies focusing on solvent choice are required to better understand iron-mediated photoredox catalysis transformations both in $[Fe(phtmeimb)_2]^+$ and in Fe photosensitizers more generally.

Here, we utilized $[Fe(phtmeimb)_2]^+$ (FePS) to drive a dehalogenation/intramolecular cyclization reaction (Figure 1) reported previously by Stephenson *et al.* with the prototypical $[Ru(bpy)_3]^{2+}$ (RuPS) and $[Ir(ppy)_2(dtb)]^+$ photosensitizers (where ppy is 2-phenyl-pyridine and dtb is 4,4'-di-*tert*-butyl-2,2'-bipyridine).[45] We interrogated the fundamental parameters which governed this visible light mediated transformation for each photosensitizer, RuPS, $[Ir(ppy)_2(bpy)]^+$ (IrPS) and FePS, in dichloromethane (CH_2Cl_2), acetonitrile (CH_3CN) and *N*,*N*-dimethylformamide (DMF). Steady-state and time-resolved spectroscopies revealed that the FePS catalyzed reaction was highly solvent dependent, with cage escape and product yields improving in low dielectric solvents. This solvent dependency was consistent with recently published data for FePS and appears to be generalizable to other organic dehalogenation reactions.[44] Experimental data also provided initial kinetic evidence for a previously reported H-atom transfer reaction between a reduced $[Ir(ppy)_2(dtb)]^+$ photosensitizers and oxidized triethylamine (TEA).[46] Finally, it was shown that the nature of the photosensitizer determined product distributions, and provided the first mechanistic and kinetic picture of a dehalogenation/intramolecular cyclization catalytic cycle.

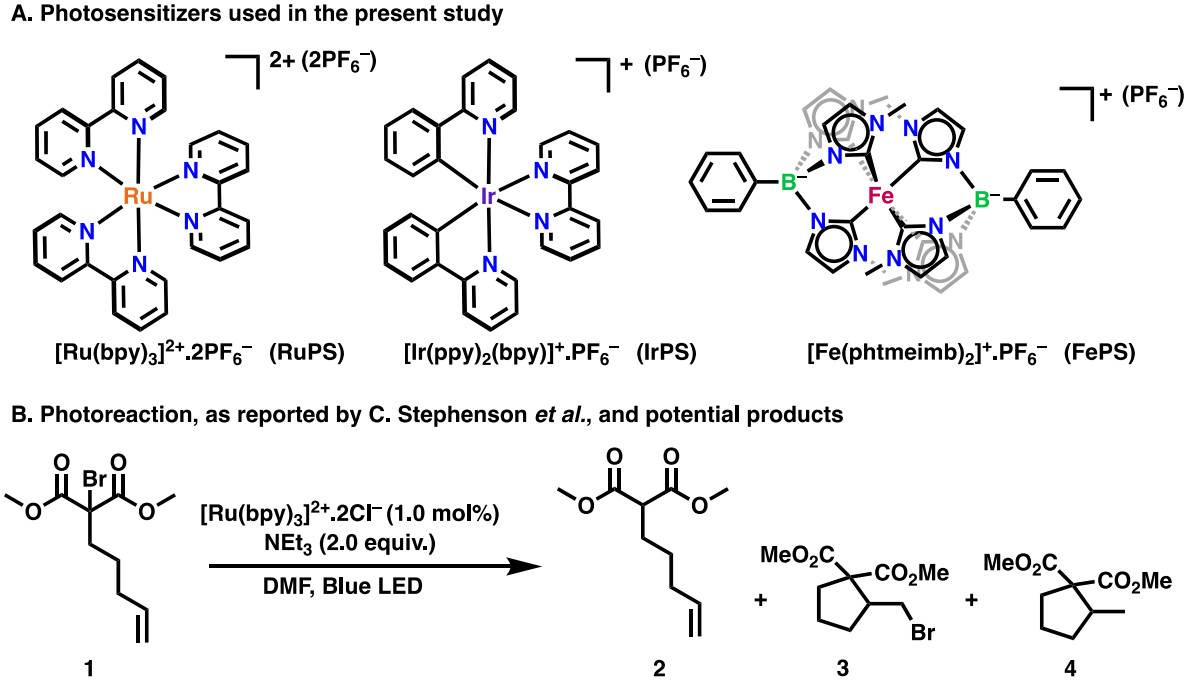

Figure 1. Photosensitizers used in the present study (a), *i.e.* $[Ru(bpy)_3]^{2+}$, $[Ir(ppy)_2(bpy)]^+$ and $[Fe(phtmeimb)_2]^+$ as well as the prototypical photoreaction, as reported by C. Stephenson *et al.*[45] (b).

Experimental

Acetonitrile 99.9% (VWR), dry acetonitrile 99.8% (Sigma-Aldrich), 5-Bromo-1-pentene 97% (Fluorochem), N-Bromosuccinimide 99% (Acros Organics), *n*-Butyllithium solution (1.6 M in hexanes) (Acros Organics), CH_2Cl_2 99% (VWR), dry CH_2Cl_2 99.8% (Sigma-Aldrich), dichlorophenylborane 97% (Acros Organics), Diethyl ether 99% (VWR), dry diethyl ether 99.5% (Acros Organic), dry *N*,*N*-Dimethylaniline ≥99.5% (Sigma-Aldrich), dry N,N-dimethylformamide 99.8% (Sigma-Aldrich), Dimethyl malonate >99% (Acros Organics), absolute Ethanol ≥99.8% (VWR), Hexamethyldisilazane 98% (Acros Organics), aqueous HCl 37% for analysis (VWR), Iridium(III) chloride hydrate (PressChem), ultra dry Iron(II) bromide 99.995% (Alfa Aesar), Lithium bromide >99% (Acros Organics), Manganese acetate dehydrate 97% (Sigma-Aldrich), 1-Methylimidazole 99% (Acros Organics), NaOH pellet for analysis (VWR), NH_4PF_6 99% (Fluorochem), 2-Phenylpyridine 97% (Acros Organics), dry Potassium *tert*-butoxide solution (1.0 M in THF) (TCI Chemicals), Potassium carbonate 98% (Acros Organics), dry Tetrahydrofuran 99.9% (Sigma-Aldrich), Tetra-*n*-butylammonium hexafluorophosphate 99% (Fluorochem), Trimethylsilyl trifluoromethanesulfonate 98% (Fluorochem), dry Triethylamine 99% (Fluorochem), dry Toluene 99.85% (Acros Organics), SiO_2 40-63 µm (Rocc) and neutral aluminum oxide Brockmann 50-200 µm 60Å (Acros Organics) were purchased from commercial suppliers and used as received.

$[Ru(bpy)_3](PF_6)_2$[47], $[Fe(phtmeimb)_2](PF_6)$[27], $Ir(ppy)_2(bpy)$,[48] *fac*-$Ir(ppy)_3$[49], dimethyl 2-bromo-2-(pent-4-en-1-yl)malonate **1**[45] and dimethyl 2-(pent-4-en-1-yl)malonate **2**[50] were synthetized according to literature procedure. The ligand tris(3-methylimidazolium-1-yl)(phenyl)borate bis(hexafluorophosphate) was synthetized according to literature procedure and then crystallized by slow diffusion of diethylether into a concentrated acetonitrile solution in a dessicator.[27, 51]

Nuclear Magnetic Resonance. NMR spectra were recorded on a Bruker AC-300 Avance II (300 MHz) or on a Bruker AM-500 (500 MHz) at 20 °C. The solvent residual peaks were used as internal standards for ^1H (δ =7.26 ppm for $CDCl_3$ and δ = 1.94 ppm for CD_3CN) and ^{13}C (δ =77.16 ppm for $CDCl_3$) chemical shift referencing. NMR spectra were processed using MNOVA. Yields were determined after column chromatography by ^1H NMR spectroscopy using 3,4,5-trimethoxybenzaldehyde as internal reference (500MHz, relaxation delay of 20 seconds).

High Resolution Mass Spectrometry. Organic compounds were analyzed using a Q-Extractive orbitrap from ThermoFisher and ionized by atmospheric-pressure chemical ionization (APCI).

UV–Visible Absorption. UV−vis absorption spectra were recorded on a Shimadzu UV-1700 with 1 cm path length quartz cuvette.

Irradiation experiments. Blue light (LIU470A, 470 nm, 4.0 mW/cm^2) and green light (LIU525A, 525 nm, 1.9 mW/cm^2) from Thorlabs were used and positioned 4-5 cm away from the sample.

Steady-State Photoluminescence. Room temperature steady-state photoluminescence (PL) spectra were recorded on a Horiba Scientific-FL-1000 fluorimeter and were corrected by calibration of the instrument's response with a standard tungsten-halogen lamp. The photoluminescence intensity was integrated for 0.1 s at 1 nm resolution and averaged over 3 scans.

Time-Resolved Photoluminescence. Nanosecond transient absorption measurements were acquired on a previously described apparatus.[52] Time-resolved PL data were acquired on a nitrogen dye laser with excitation centered at 445 nm. Pulsed light excitation was achieved with a Photon Technology International (PTI) GL-301 dye laser that was pumped by a PTI GL-3300 nitrogen laser. The PL was detected by a Hamamatsu R928 PMT optically coupled to a ScienceTech Model 9010 monochromator terminated into a LeCroy Waverunner LT322 oscilloscope. Decays were monitored at the PL maximum and averaged over 180 scans.

Nanosecond Transient Absorption Spectroscopy. Nanosecond transient absorption measurements were acquired on a previously described apparatus.[53] Briefly, a Q-switched, pulsed Nd:YAG laser (Quantel USA (BigSky) Brilliant B 5−6 ns full width at half-maximum (fwhm), 1 Hz, ~ 10 mm in diameter) was doubled to 532 nm. The laser irradiance at the sample was attenuated to 2 mJ/pulse. The probe lamp consisted of a 150 W xenon arc lamp and was pulsed at 1 Hz with 70 V during the experiment. Signal detection was achieved using a monochromator (SPEX 1702/ 04) optically coupled to an R928 photomultiplier tube (Hamamatsu) at a right angle to the excitation laser. Transient data were acquired with a computer-interfaced digital oscilloscope (LeCroy 9450, Dual 330 MHz) with an overall instrument response time of ~10 ns. An average of 30 laser pulses was acquired averaged at each wavelength of interest over the 370−800 nm range. Intervals of 10 nm were used for wavelength between 370 and 600 nm and intervals of 20 nm were used between 600 and 800 nm. Transient absorption changes at selected wavelengths used to calculate cage escape yields were monitored as an average of 90-150 laser pulses.

Data analysis. Data analysis for all experiments was performed using *OriginLab, version 9.0.* Data fitting was preformed using a Levenberg-Marquardt iteration method.

Stern-Volmer experiments. A solution of the desired photosensitizer with an absorbance of ~ 0.1 at the excitation wavelength was prepared in the desired solvent. Various quencher solutions with concentration ranging from 0.05 to 0.5 M were prepared in the desired solvent containing. The desired quencher was gradually added to a solution of the photosensitizer and the excited-state quenching was monitored by steady-state photoluminescence. The decrease of photoluminescence can be directly related to the concentration of quencher and the respective Stern-Volmer plots were extrapolated using **equation 1**.

Femtosecond Transient Absorption Spectroscopy. Samples for femtosecond transient absorption (fsTAS) measurements were dissolved in argon purged anhydrous ACN or DCM. All measurements were conducted in a 2 mm quartz cuvette under argon atmosphere. Ultrafast experiments were performed with an amplified Ti/sapphire laser system (Clark MXR CPA2101 and CPA2110, 1kHz, FWHM = 150 fs, λ_{exc} = 500 nm, 300 - 700 nJ per pulse) with TA pump/probe Helios detection system from Ultrafast Systems. White light was generated focusing a fraction of the fundamental 775 nm output onto a 2 mm sapphire disk (~430−760 nm). A magic angle configuration was employed to avoid rotational dynamics. Excitation pulses of 500 nm were generated by a NOPA. Bandpass filters with ± 5 or ± 10 nm were used to ensure low spectral width and to exclude 775 nm photons. To analyze transient absorption data, we use a suggested procedure and employed global analysis using the R-package TIMP and GloTarAn.[54-56]

Time-Resolved Infrared Spectroscopy. Time-resolved infrared spectroscopic experiments were conducted using a previously described experimental setup.[57]

Synthesis of 3. A 25 mL round bottom flask was charged with dimethyl 2-bromo-2-(pent-4-en-1-yl)malonate **1** (0.9100 g, 3.26 mmol, 1 eq.), LiBr (1.6988 g, 19.56 mmol, 6 eq.) and [Ir(ppy)$_3$] (0.0213 g, 0.0326 mmol, 0.01 eq.) and equipped with a rubber septum and magnetic stir bar. The flask was placed under static vacuum for 15 minutes and then filled with argon atmosphere. 15 mL of dry DMF were added and the resulting solution was degassed three times by freeze and pump technique and then placed under argon. The reaction mixture was stirred and illuminated for 24h at a distance of 4-5 cm with a Thorlab blue lamp. Afterwards, the reaction mixture was poured in a separation funnel with 50 mL of distilled water and 50 mL of Et_2O were added. The aqueous layer was extracted three times with 50 mL of Et_2O. The organic phases were combined, dried over Na_2SO_4, filtered, and evaporated under reduced pressure. The crude was purified by flash chromatography on SiO_2 (diethylether/petroleum ether: 5/95). The desired fractions were collected and evaporated under reduced pressure to afford dimethyl 2-(bromomethyl)cyclopentane-1,1-dicarboxylate **3** as a colorless oil (0.650 g, 2.33 mmol) with 71 % yield. HRMS (*m/z*) (APCI$^+$) Calculated for $C_{10}H_{16}O_4{}^{79}Br$ *m/z* = 279.02265 [M+H]$^+$. Found *m/z* = 279.02244. ^{1}H NMR ($CDCl_3$, 500 MHz) δ (ppm) 3.74 (s, 3H, **H$_6$**), 3.73 (m, 1H, **H$_1$**), 3.71 (s, 3H, **H$_6$'**), 3.26 (dd, $J_{H1'-H1}$ = 10.4 Hz, $J_{H1'-H2}$ 9.8 Hz, 1H, **H$_{1'}$**), 2.95-2.89 (m, 1H, **H$_2$**), 2.45 (m, 1H, **H$_5$**), 2.23-2.11 (m, 2H, **H$_3$** and **H$_{5'}$**), 1.90-1.81 (m, 2H, **H$_4$**), 1.69-1.58 (m, 2H, **H$_{3'}$** and **H$_{4'}$**); ^{13}C NMR ($CDCl_3$, 75 MHz) δ (ppm) 172.14, 170.95, 63.06, 52.93, 52.68, 48.82, 35.21, 34.36, 30.89, 22.30.

Synthesis of 4. $Mn(OAc)_3$ (0.536 g, 2.0 mmol, 2 eq.), dimethyl 2-(pent-4-en-1-yl)malonate **2** (0.200 g, 1.0 mmol, 1 eq.) and 50 mL of dry degassed ethanol were added to a 100 mL round bottom flask. The reaction mixture was stirred at 70 °C under argon for 24 hours. After completion, the reaction mixture was filtered on a porosity 3 frit and the filtrate was poured in a separation funnel with 50 mL of distilled water and 50 mL of Et_2O. The aqueous layer was extracted three times with 50 mL of Et_2O. The organic phases were combined, dried over Na_2SO_4, filtered, and evaporated under reduced pressure. The crude was purified by flash chromatography on SiO_2 (diethylether/petroleum ether: 5/95). The desired fractions were collected and evaporated under reduced pressure to afford dimethyl 2-methylcyclopentane-1,1-dicarboxylate **4** as a colorless oil (0.084 g, 0.42 mmol) with 42% yield. HRMS (*m/z*) (APCI$^+$) Calculated for $C_{10}H_{17}O_4$ *m/z* = 201.11214 [M+H]$^+$. Found *m/z* = 201.11218; ^{1}H NMR ($CDCl_3$, 500 MHz) δ (ppm) 3.72 (s, 3H, **H$_6$**), 3.70 (s, 3H, **H$_{6'}$**), 2.67 (ddq, J_{H2-H3} = 8.9 Hz, $J_{H2-H3'}$ = 7.0 Hz, J_{H2-H1} = 7.0 Hz, 1H, **H$_2$**), 2.44 (ddd, $J_{H5-H5'}$ = 13.9 Hz, J_{H5-H4} = 8.8 Hz, $J_{H5-H4'}$ = 7.6 Hz, 1H, **H$_5$**), 2.02 (ddd, $J_{H5'-H5}$ = 13.9 Hz, $J_{H5'-H4'}$ = 9.3 Hz, 4.7 Hz, 1H, **H$_{5'}$**), 1.95-1.78 (m, 2H, **H$_3$ and H$_4$**), 1.61-1.52 (m, 1H, **H$_{4'}$**), 1.43-1.36 (m, 1H, **H$_{3'}$**), 0.97 (d, J_{H-H} = 7.0 Hz, 3H, **H$_1$**); ^{13}C NMR ($CDCl_3$, 75 MHz) δ (ppm) 173.24, 172.05, 63.85, 52.54, 52.12, 40.99, 34.12, 33.56, 23.04, 16.62. ^{1}H and ^{13}C NMR data were in agreement with those reported.[58]

Photocatalytic conversion of 1 to 2, 3 and 4. A 10 mL round bottom flask was charged with **1** (0.0549 g, 0.2 mmol, 1 eq.) and the photosensitizer (2 µmol, 0.01 eq.) and equipped with a rubber septum and magnetic stir bar. The flask was placed under static vacuum for 15 minutes and then filled with argon atmosphere. A solution of dry triethylamine (0.5 mL) in dry solvent (10 mL) prepared in a flame-dried 25 mL Schlenk was degassed by three freeze-pump-thaw cycles and placed under argon. 2 mL of this solution were then added to the reaction flask and the reaction mixture was stirred and illuminated for 24h at a distance of 4-5 cm with a Thorlab LED. After reaction, the mixture was diluted with 50 mL of Et_2O and was then filtered on a fine porosity frit. The filtrate was poured in a separation funnel with 50 mL of 0.1M HCl. The aqueous layer was extracted three times with 50 mL of Et_2O. The organic phases were combined, dried over Na_2SO_4, filtered, and evaporated under reduced pressure and dried under vacuum to afford a colorless oil. The yield was determined by ^{1}H NMR spectroscopy using 3,4,5-trimethyoxybenzaldehyde as internal standard (500 MHz, relaxation delay of 20 seconds). ^{1}H NMR and ^{13}C NMR data were in agreement with those reported.[45]

Results and discussion

The three photosensitizers were synthesized according to known procedures.[27, 44, 47, 48] Spectroscopic characterization of their UV-Visible light absorption and photoluminescence (PL) response are shown in **Figure 2**. The intense MLCT molar absorption coefficient of RuPS – 12,000 $M^{-1}cm^{-1}$ at 450 nm in CH_3CN – makes it the most effective light harvester in the visible spectral region amongst the series of photosensitizers studied here. The prototypical iridium(III) complex IrPS displays similar MLCT excited state properties, albeit with significantly lower molar absorptivities.[59, 60] In both Ru(II) and Ir(III)-based sensitizers, the MLCT character of the excited state formally oxidizes the metal center by transferring an electron to the most easily reduced ancillary ligand.[61-63] For FePS, the excited-state was previously assigned as a ligand-to-metal charge transfer (LMCT), hence formally oxidizing the ancillary ligand and reducing the metal center from Fe(III) to Fe(II).[27] The room temperature PL for all photosensitizers is well described by

radiative and non-radiative relaxation from a single thermally-equilibrated excited state, in agreement with Kasha's rule. Solvatochromic PL with spectral shifts of 715 cm^{-1} for RuPS, 628 cm^{-1} for FePS and 416 cm^{-1} for IrPS were observed when the solvent was changed from CH_2Cl_2 to DMF. Photoluminescent excited-states decays were well described by a first-order kinetic model with lifetimes (τ) of ~ 2 ns for $[Fe(phtmeimb)_2]^{+*}$ (FePS*) in all solvents investigated. Excited-state lifetimes for $[Ru(bpy)_3]^{2+*}$ (RuPS*) ranged from ~ 1 µs in DMF to 755 ns in CH_2Cl_2, as explained by the decreased energy gap between the ^{3}MLCT excited-state and the ligand-field (LF) state.[63-67] For $[Ir(ppy)_2(bpy)]^{+*}$ (IrPS*), the excited-state lifetimes were also sensitive to the solvent identity and varied from ~300 ns in polar solvents (CH_3CN and DMF) to 700 ns in CH_2Cl_2. The ground and excited-state properties are gathered in **Table 1**.

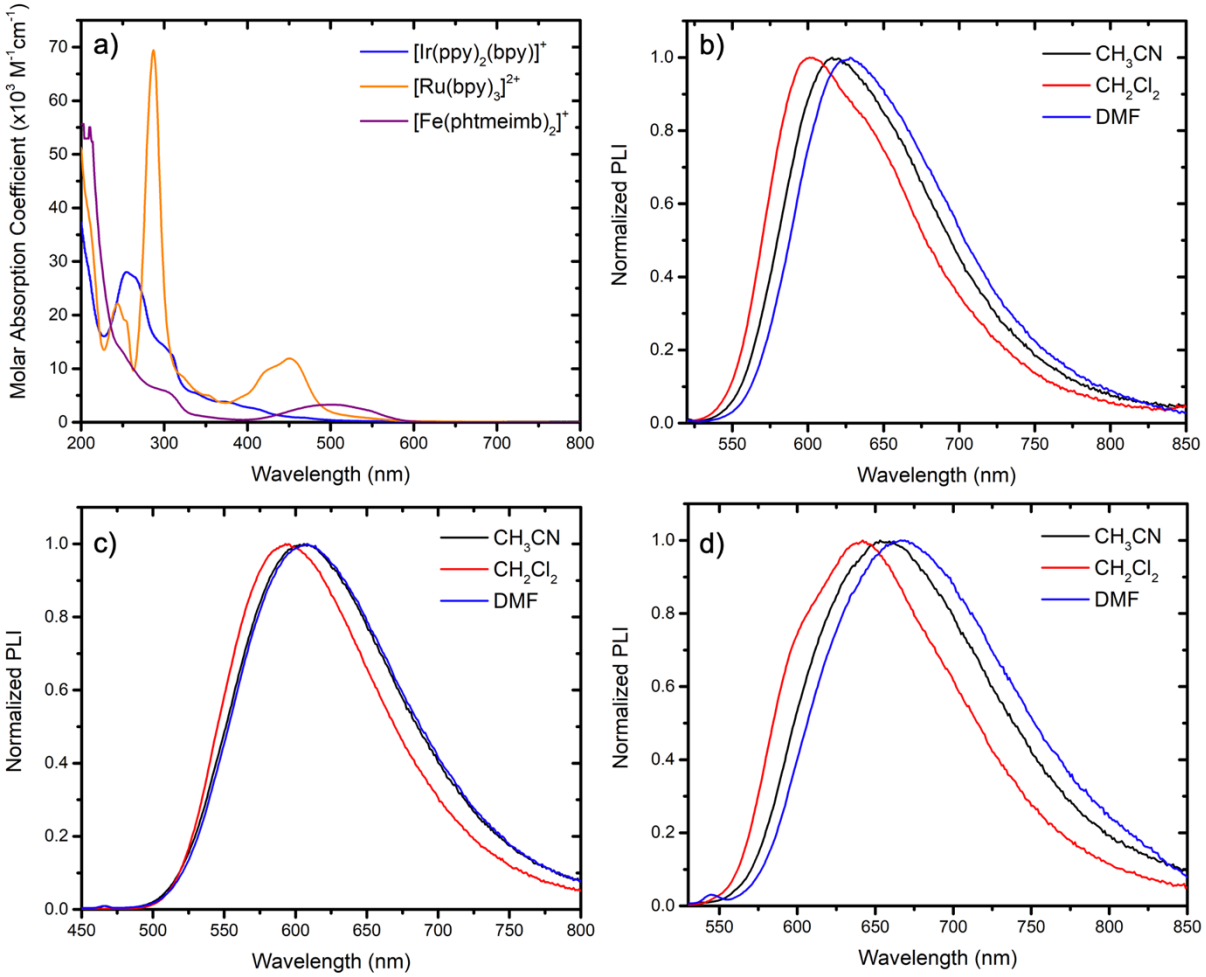

Figure 2. Absorption spectra (a) recorded in CH_3CN and photoluminescence spectra of $[Ru(bpy)_3]^{2+}$ (b), $[Ir(ppy)_2(bpy)]^+$ (c) and $[Fe(phtmeimb)_2]^+$ (d) in DMF (blue), CH_3CN (black), and CH_2Cl_2 (red) recorded at room temperature.

Table 1. Photophysical and electrochemical data of $Ru(bpy)_3]^{2+}$, $[Ir(ppy)_2(bpy)]^+$ and $[Fe(phtmeimb)_2]^+$ in the indicated solvent.

Complex	Solvent	Abs[a] (ε)[b]	PL_{max}[a]	τ[c]	$E_{1/2}(PS^{+/0})$[d]	$E_{1/2}(PS^{*/+})$[d]	$E_{1/2}(PS^{0/-})$[d]	$E_{1/2}(PS^{*/-})$[d]
	CH_2Cl_2		601	430 (755)				
$[Ru(bpy)_3]^{2+}$	CH_3CN	450 (12000)	616	170 (890)	1.50[e]	–0.64[e]	–1.11[e]	1.03[e]
	DMF		628	235 (1020)				
	CH_2Cl_2		593	170 (700)				
$[Ir(ppy)_2(bpy)]^+$	CH_3CN	410 (2530)	606	110 (365)	1.56[f]	–0.84[f]	–1.16[f]	1.24[f]
	DMF		608	155 (325)				
	CH_2Cl_2		642	2.47 (2.41)[g]				
$[Fe(phtmeimb)_2]^+$	CH_3CN	500 (3300)	653	2.12 (2.07)[g]	0.88[h]	–1.25[h]	–0.55[h]	1.58[h]
	DMF		669	1.70 (1.65)[g]				

[a] Wavelength in nm. [b] Molar extinction coefficient in $M^{-1}cm^{-1}$. [c] Excited-state lifetime in ns. Values determined under air with values for argon-purged solutions in parenthesis. [d] V vs NHE. [e] from ref [68]. [f] from ref [48]. [g] from ref [44]. [h] from ref [27].

Excited-state quenching of the transition metal photosensitizers by the sacrificial donor triethylamine (TEA) was investigated under argon in CH_2Cl_2, CH_3CN and DMF (**Figure 3a-c and SI)**. Stern-Volmer plots of the quenching data, **Figure 3d**, had a linear dependence on TEA concentration, indicative of dynamic quenching with no static contributions. Linear regression of the data, according to **equation 1**, generated slopes that were used to calculate quenching rate constants (k_q) in the ~10^6 $M^{-1}s^{-1}$ range for RuPS, ~10^7 $M^{-1}s^{-1}$ for IrPS and the much larger rate constant of ~10^9 $M^{-1}s^{-1}$ for FePS. These quenching rate constants are reported in **Table 2**.

$$\frac{\sum(PLI_0)}{\sum(PLI)} = 1 + K_{SV}[Q] = 1 + k_q\tau_0[Q] \qquad \text{Eq. 1}$$

Table 2. Quenching rate constant for the excited-state reactivity of the indicated photosensitizer with TEA in CH_2Cl_2, CH_3CN and DMF

		k_q (x10^9 $M^{-1}s^{-1}$)		
	ΔG (meV)[a]	CH_2Cl_2	CH_3CN	DMF
$[Ru(bpy)_3]^{2+}$	+190 (-1)	0.009	0.001	0.002
$[Ir(ppy)_2(bpy)]^+$	-2 (-220)	0.016	0.040	0.048
$[Fe(phtmeimb)_2]^+$	-360 (-560)	5.1	8.1	3.4

[a] Calculated using E^0 ($TEA^{\bullet+}$/TEA) = 1.22 V or 1.02 V (values in parenthesis) vs NHE to represent upper and lower limits.

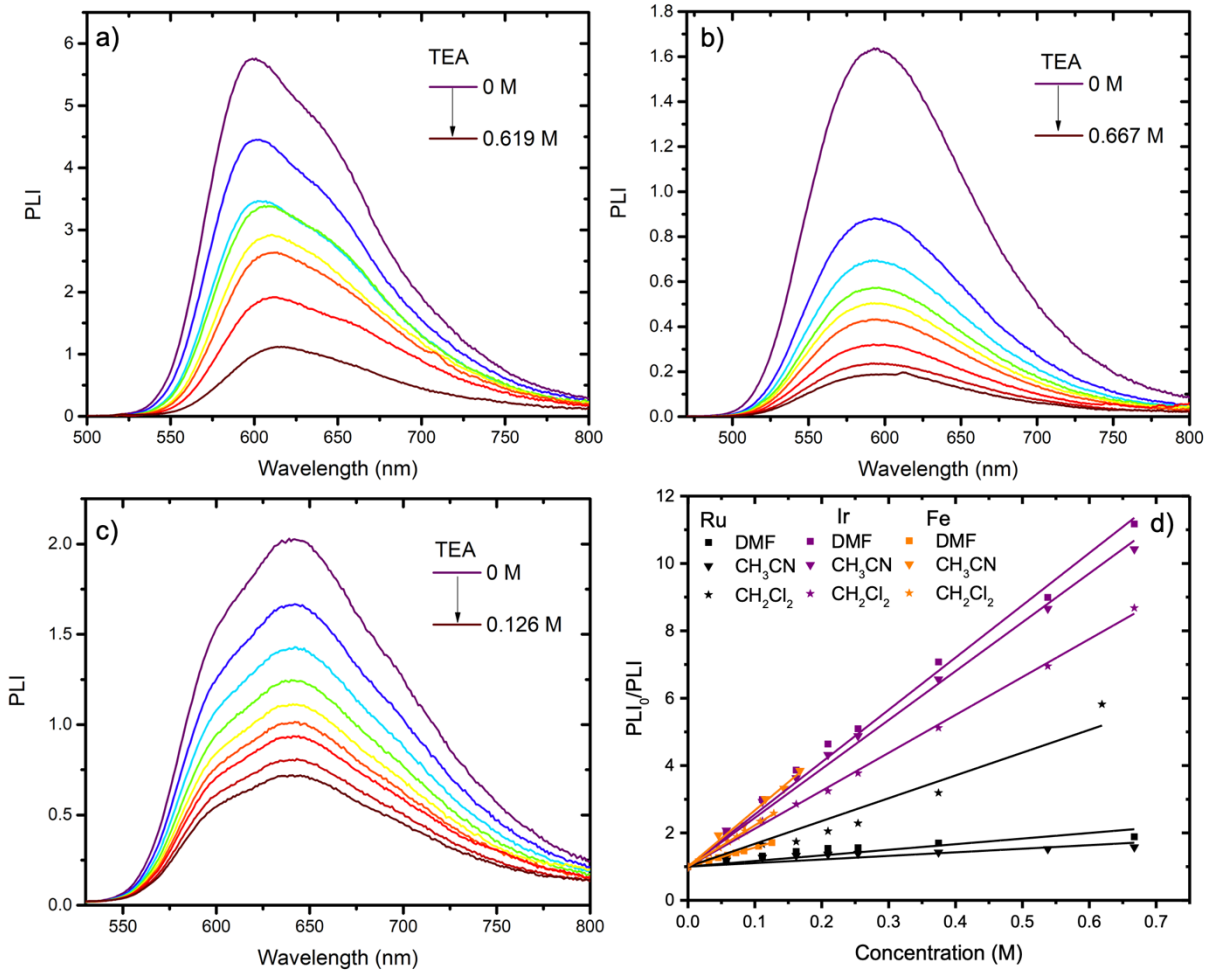

Figure 3. Excited-state quenching of $[Ru(bpy)_3]^{2+}$ (a), $[Ir(ppy)_2(bpy)]^+$ (b) and $[Fe(phtmeimb)_2]^+$ (c) by TEA in CH_2Cl_2 under argon at room temperature. The corresponding Stern-Volmer plots, including those recorded in CH_3CN and DMF are presented in panel d.

The thermodynamics of the electron transfer step account for the differences in quenching rate constants between the photosensitizers. Literatures values for the $TEA^{\bullet+/0}$ reduction potentials range from 1.02 V vs NHE to 1.22 V vs NHE, which leads to significant uncertainty in the free energy for electron transfer ($-\Delta G° = E_{1/2}(PS^{*/-}) - E_{1/2}(TEA^{\bullet+/0})$). Nonetheless, reductive quenching of FePS* by TEA is always exothermic even by assuming the smallest $TEA^{\bullet+/0}$ reduction potential. For IrPS*, the estimated driving force is in the –0.002 and –0.22 eV range, either being near thermoneutral or exergonic. For RuPS*,

however, –ΔG° is at best thermoneutral (–0.001 eV) and at worst endergonic by 0.19 eV, which may account for the smaller quenching rate constants.

Nanosecond transient absorption spectroscopy was used identify the products of the excited-state quenching. In all cases, quenching of the PS excited states by TEA resulted in absorption changes consistent with formation of the singly reduced photosensitizers (PS^{-}), **Figure 4**, with rate constants consistent with those obtained from Stern-Volmer analysis indicating that PS^{-} was a primary photochemical product. The much larger quenching rate constants for FePS* could not be time resolved. Cage escape yields (ϕ_{CE}) of the [$PS(e^{-})$;$TEA^{\bullet+}$] encounter complex to produce the charge separated PS^{-} and $TEA^{\bullet+}$ products after reductive quenching in CH_2Cl_2, CH_3CN and DMF were determined by comparative actinometry methods, **equations 2-3**. In these determinations, RuPS was used as referenced actinometer, as well as photosensitizer.

$$\Phi_{CE} = \frac{\phi}{\%\ PL\ Quenched} \qquad Eq.2$$

$$\phi = \left(\frac{\frac{\Delta A_{PS^-}}{\Delta \varepsilon_{PS^-}}}{\frac{\Delta A_{ES_{ref}}}{\Delta \varepsilon_{ES_{ref}}}}\right)\left(\frac{1-10^{-Abs_{PS}(\lambda_{exc})}}{1-10^{-Abs_{ref}(\lambda_{exc})}}\right) \qquad Eq.3$$

In **equations 2-3**, the maximum absorption changes generated from PS^{-} was compared to the absorption maxima of the excited state of the RuPS reference, ES_{ref}, and normalized by their respective absorptances at the excitation wavelength (λ_{exc} = 532 nm). Final ϕ_{CE} values were obtained by comparing the relative ratio of PS^{-} produced to the percentage of quenched PL (%PL). For RuPS, ϕ_{CE} increased with solvent polarity – lower yields of 0.15 ± 0.03 were found for CH_2Cl_2, moderate yields of 0.39 ± 0.03 were found in CH_3CN, and much higher values were determined in DMF, ϕ_{CE} = 0.58 ± 0.08. This observation is in line with the expectation that polar solvents are better at stabilizing charged species.

Interestingly, ϕ_{CE} values determined for FePS exhibited the opposite trend as those of RuPS, *i.e.* higher yields were measured in low polarity solvents (ϕ_{CE} = 0.21 ± 0.05 in CH_2Cl_2) whereas lower yields of were measured in DMF (ϕ_{CE} = 0.09 ± 0.03) and CH_3CN (negligible ϕ_{CE}). Ultrafast femtosecond transient absorption data was collected for FePS to interrogate this trend in cage escape yields. In CH_2Cl_2, light excitation of FePS with 0.35 M TEA induced spectral changes that indicated simultaneous loss of the LMCT excited-state and formation of the monoreduced photosensitizer (**Figure 5**). In CH_3CN, even though sub-nanosecond excited-state quenching was evident, no spectral signatures of the $FePS^{-}$ were observed. This observation indicated that in the high polarity CH_3CN, the monoreduced photosensitizer population underwent quantitative geminate recombination, precluding cage escape and long-lived photoproduct formation.[21]

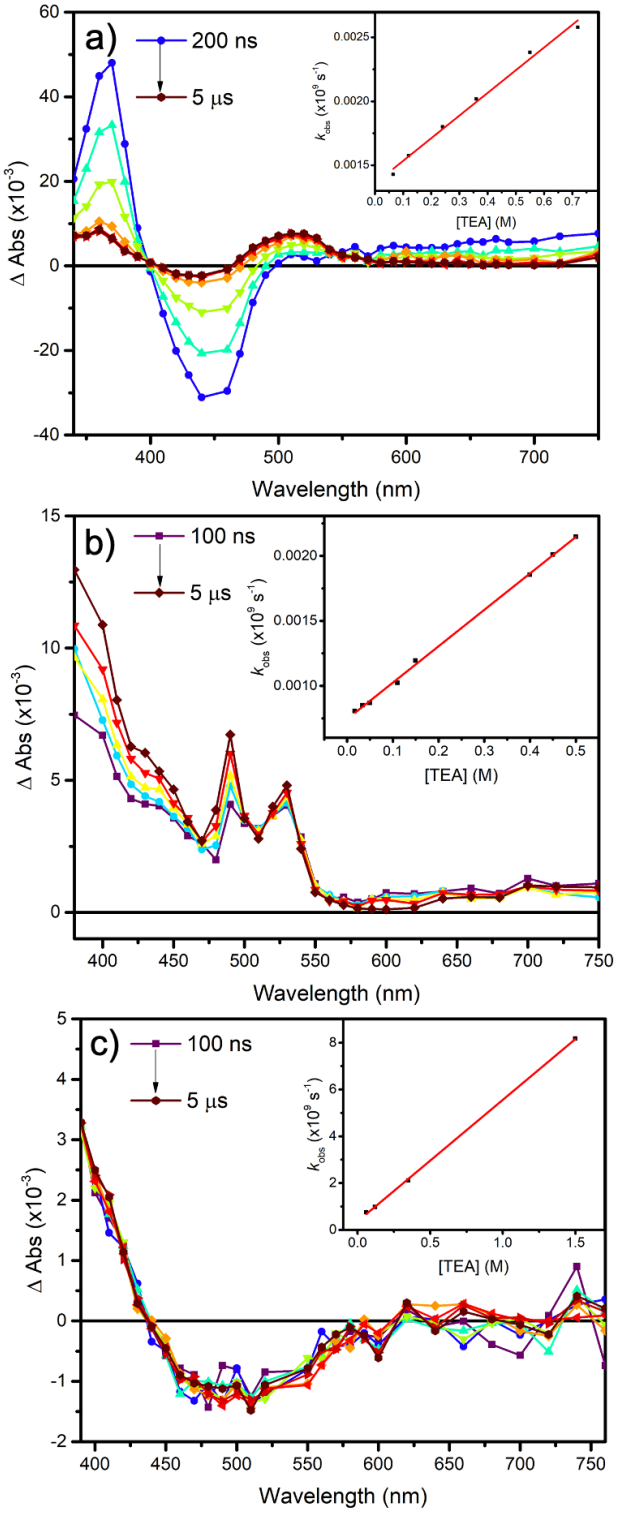

Figure 4. Nanosecond transient absorption spectra measured at the indicated delay times following pulsed-light excitation of $[Ru(bpy)_3]^{2+}$ (a), $[Ir(ppy)_2(bpy)]^{+}$ (b) and $[Fe(phtmeimb)_2]^{+}$ (c). The spectra were measured in CH_3CN for $[Ru(bpy)_3]^{2+}$ and $[Ir(ppy)_2(bpy)]^{+}$ and in CH_2Cl_2 for $[Fe(phtmeimb)_2]^{+}$. Experiments were carried out under argon at room temperature in the presence of 200 mM TEA. The inset shows the rate constant for the formation of monoreduced $[Ru(bpy)_3]^{+}$, $[Ir(ppy)_2(bpy)]$ and $[Fe(phtmeimb)_2]$ (recorded on the femtosecond time scale, vide infra).

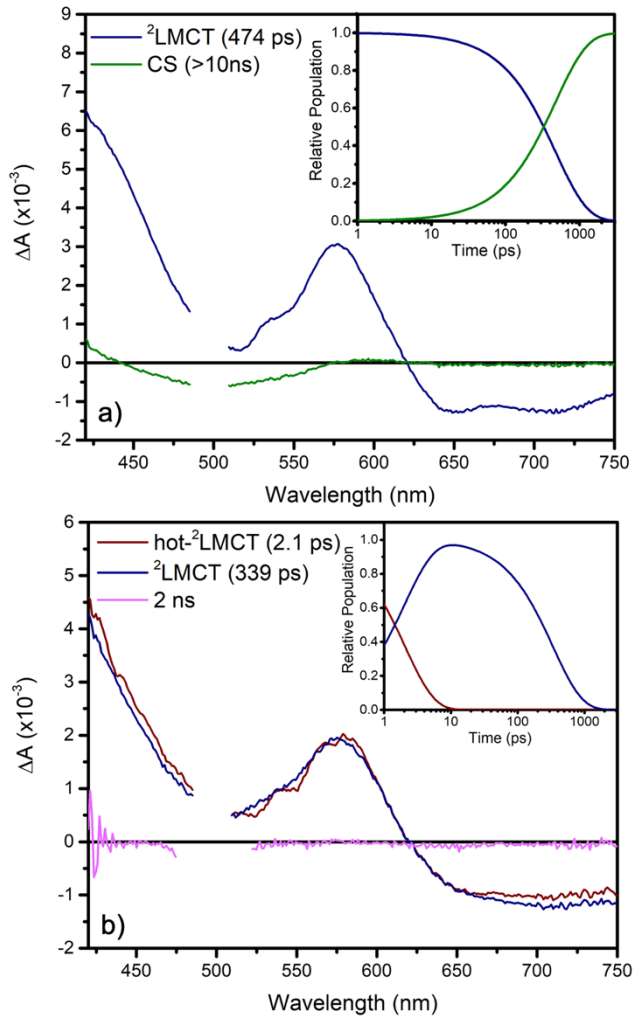

Figure 5. Femtosecond transient absorption spectra recorded at the indicated delay times after pulsed 500 nm laser excitation of $[Fe(phtmeimb)_2]^+$ (7 x 10^{-4} M) in argon saturated 0.35M TEA in CH_2Cl_2 (a) and CH_3CN (b) at room temperature. The insets represent the relative populations of the excited and charge separated.

The solvent conditions that promoted the largest cage escape yields, as determined by Stern-Volmer experiments and transient spectroscopies, were utilized to study the selected dehalogenation reaction, as reported by C. Stephenson *et al.* (**Figure 1**).[45] The dehalogenation/cyclization reaction was investigated in CH_2Cl_2, CH_3CN and DMF under argon with blue or green light irradiation using TEA as a sacrificial donor. The resulting yields of compounds **1-4** were determined by quantitative ^{1}H NMR and are gathered in **Figure 6** and in **Table S1**.

For RuPS and IrPS, illumination of the reaction mixture resulted in complete transformation of the substrate **1** to form the halogenated 5-membered ring product (**3**) and the dehalogenated 5-membered ring analogue (**4**). The nature and ratio of the products were largely independent of solvent (CH_2Cl_2, CH_3CN and DMF) or irradiation wavelength (**Figure 6**, **Table 3** and **S1**). In all cases, **3** was the dominant product over **4** by ratios of 2:1 to 4:1.

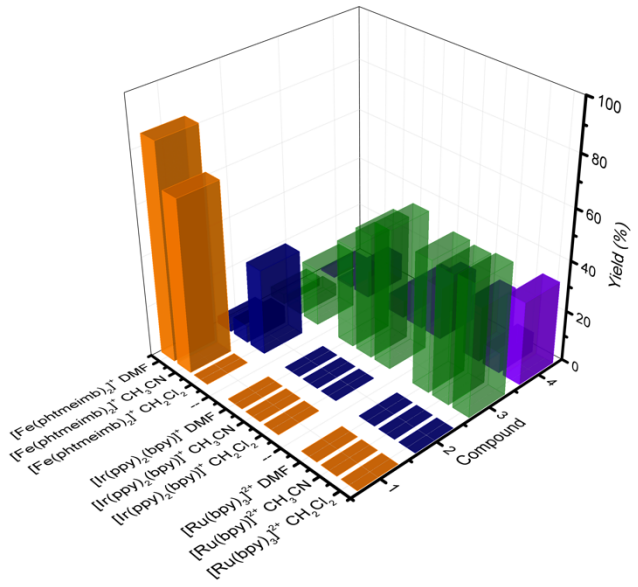

Figure 6. Percent yields of compounds **1-4** obtained with blue-light mediated dehalogenation/cyclization reaction using the following conditions: PS (1 mol%), TEA (3.5 eq., 0.7 mmol), solvent (2 mL), under inert atmosphere and irradiation for 24h.

Table 3. Yields of compounds **1-4** obtained with blue light irradiation. Tabulated values obtained with green light irradiation are presented in **table S1**.

	CH_2Cl_2 (1/2/3/4) (%)	CH_3CN (1/2/3/4) (%)	DMF (1/2/3/4) (%)
$[Ru(bpy)_3]^{2+}$	0/0/52/33	0/0/51/8	0/0/52/22
$[Ir(ppy)_2(bpy)]^+$	0/0/55/21	0/0/49/16	0/0/40/7
$[Fe(phtmeimb)_2]^+$	0/34/23/11	68/7/5/1	85/3/4/1

Conditions : PS (1 mol%), TEA (3.5 eq., 0.7 mmol), solvent (2 mL), blue light, under inert atmosphere and under irradiation for 24h.

Recently, Connell *et al.* reported that the excited state of $[Ir(ppy)_2(dtb)]^+$, where dtb is 4,4'-(^{t}Bu)$_2$-2,2'-bipyridine reacts with TEA to generate the singly reduced photosensitizer with an electron located on the dtb ligand, $[Ir(ppy)_2(dtb^{\bullet-})]$.[46] It was proposed that ($dtb^{\bullet-}$) extracts a hydrogen atom from $TEA^{\bullet+}$ by a concerted proton coupled electron transfer or a step-wise proton coupled electron transfer mechanism. This hydrogenated photosensitizer was shown to be a more potent reducing species than the initial $[Ir(ppy)_2(dtb)]^+$. Here, similar steady-state illumination experiments (using blue LED) of IrPS in argon purged CH_3CN in the presence of 1M TEA led to the expected excited-state quenching of the PL intensity with a maximum at 605 nm for early stages of the photolysis experiment. Following steady-state illumination, a new PL spectra emerged with maxima at 513 and 481 nm, similar to observations reported by Connell *et al.*, also indicating that $[Ir(ppy)_2(bpy^{\bullet-})]$ ($IrPS^-$) was reactive towards TEA or $TEA^{\bullet+}$ via H-atom transfer to generate the hydrogenated Ir photosensitizer ($IrPS^H$)(**Figure S5**).

More direct evidence of such PCET reactivity was obtained from TEA titration experiments into an IrPS solution with transient absorption characterization. Single wavelength kinetic data monitored at 420 nm following excited-state quenching showed biexponential behavior (**Figure 7a**). The faster kinetic

component was first-order in [TEA] with a calculated rate constant of 1.6 x 10^8 M^{-1} s^{-1} assigned to the reductive quenching step (**Figure 7b**). The much slower kinetic process, occurring on the microsecond time scale, showed a marked inverse first-order behavior with respect to [TEA], **Figure 7b**, and was tentatively assigned as the H-atom transfer from $TEA^{\bullet+}$ to $IrPS^{-}$, **Figure 7c**. This inverse concentration dependence and the fact that the relative amplitude of the absorption changes associated with this step decreased with increasing [TEA] is suggestive of a competitive pathway involving $TEA^{\bullet+}$ and TEA. As [TEA] increases, the deprotonation pathway of $TEA^{\bullet+}$ by TEA to produce the radical $TEA^{\bullet}$,**Figure 7d**, begins to compete kinetically with H-atom transfer to $IrPS^{-}$. It remains an open question of whether these competitive reaction pathways following excited-state quenching of IrPS by TEA is relevant for the photoredox catalysis presented here. Such H-atom transfer chemistry was not observed for RuPS and FePS.

In stark contrast with results obtained with RuPS and IrPS, the conversion of starting material **1** to products by FePS was quantitative only when the reaction was performed in CH_2Cl_2; whereas in the higher polarity CH_3CN and DMF, reaction yields were less than 30% after 24-hours of illumination. This significant solvent-dependency in the overall conversion efficiencies coincides with the small cage escape yields measured by transient absorption spectroscopy in high polarity solvents. Furthermore, FePS exhibited a unique chemoselectivity when compared with RuPS and IrPS, as the linear dehalogenated product **2** was produced in concentrations similar to **3**, both of which were dominant products relative to **4**.

Time-resolved infrared (TRIR) spectroscopy was performed to provide additional mechanistic insights into the RuPS and FePS photocatalyzed dehalogenation reactions.[57] TRIR allowed monitoring of the reactants and transient radical intermediates following pulsed light excitation with sub-microsecond kinetic resolution. Reference IR spectra of the substrate (**1**) and the products (**2-4**) were recorded in the carbonyl stretching region (**Figure 8a**). IR absorbance peaks at 1745 cm^{-1} with a shoulder at 1763 cm^{-1} were observed for compound **1**. The dehalogenated linear analogue **2** absorbed at 1733 cm^{-1} and 1751 cm^{-1} whereas both cyclic analogues, *i.e.* compounds **3** and **4** absorbed at 1730 cm^{-1} and 1728 cm^{-1} respectively.

In experiments performed using concentration conditions relevant to photoredox catalysis, pulsed light excitation of a solution containing RuPS, TEA and **1** resulted in absorption changes that were consistent with the consumption of **1**, as evidenced by the bleach at 1744 cm^{-1}, and the formation of a cyclic product, as evidenced by a slower growth of a positive absorption change around 1728 cm^{-1}. The close resemblance of the IR spectra of **3** and **4** precluded critical differentiation of the formed products from TRIR experiments. In the case of FePS, lower cage escape yields (0.21 ±0.05) and the short FePS* lifetime led to inefficient reactivity with TEA as the sacrificial electron donor that precluded spectroscopic monitoring of reaction intermediates. Previous studies showed cage escape yields with N,N-dimethylaniline (DMA) as an alternate sacrificial electron donor to be significantly larger (ϕ_{CE} = 0.60 ±0.09),[44] which allowed TRIR experiments to be performed. Pulsed light excitation of a solution containing FePS, DMA and **1** resulted in absorption changes that were consistent with the consumption of **1** as evidenced by the bleach at 1744 cm^{-1}, and a positive absorption change around 1752 cm^{-1} that coincided with the steady-state FTIR of the linear dehalogenated analogue **2**. Spectral features expected for the cyclic products **3** and **4** were not unambiguously identified therefore indicating a pathway that does not result in cyclization of the radical intermediate $\mathbf{2}^{\bullet}$. Kinetic studies were conducted in key spectral regions and analysed under pseudo-first order conditions relative to the concentration of substrate **1**, **Figure 9**. The kinetics measured with RuPS as the photosensitizer were complex and globally treated with a tri-exponential model tentatively assigned to three sequential steps in the catalytic cycle: 1) electron transfer from PS^{-} to **1**, 2) cyclization of $\mathbf{2}^{\bullet}$ to form $\mathbf{4}^{\bullet}$, and 3) bromine atom transfer from **1** to $\mathbf{4}^{\bullet}$ to give the final product **3**.

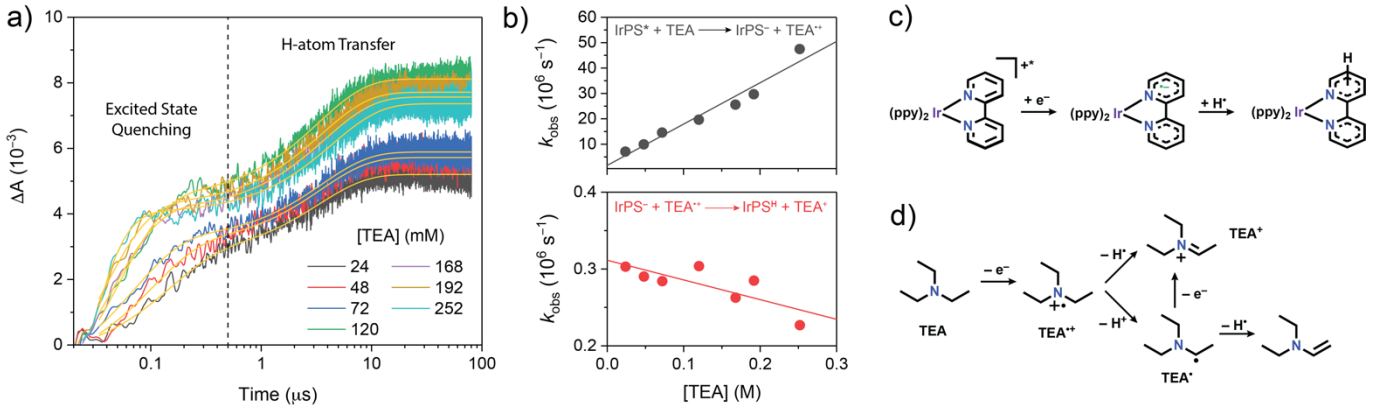

Figure 7. a) Single wavelength kinetics traces measured for $[Ir(ppy)_2(bpy)]^+$ in CH_3CN at 420 nm after pulsed 450 nm excitation at the indicated amounts of titrated TEA. b) Observed rates measured for the indicated reactions versus [TEA]. c) Related reductive quenching of $[Ir(ppy)(bpy)]^{+\bullet}$ to generate the monoreduced [Ir(ppy)(bpy)], which is followed by H-atom transfer to the reduced bipyridine ligand. d) Cascade chemistry associated with $TEA^{\bullet+}$ when TEA is oxidized by one electron.[69-73]

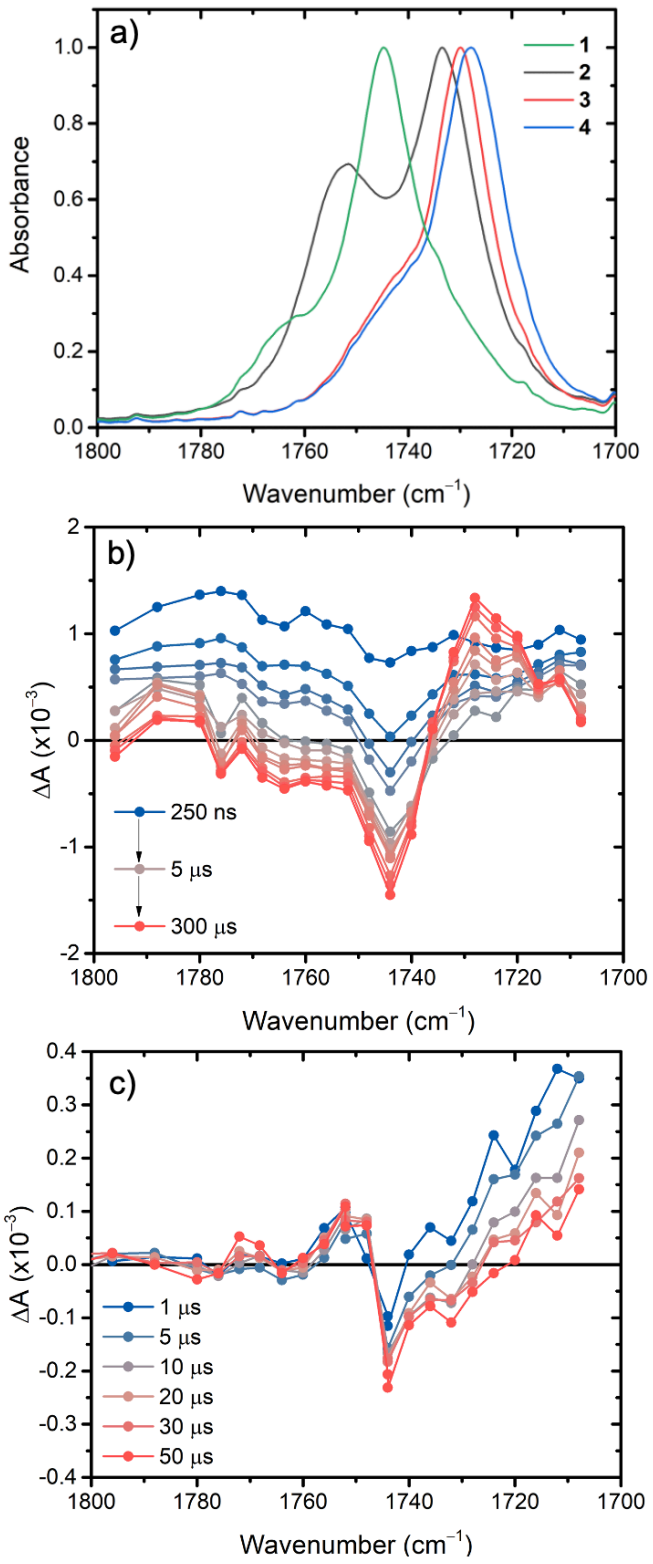

Figure 8. (**a**) Normalized Fourier transform infrared (FTIR) spectra of the indicated species. TRIR absorption changes measured after a pulsed 500 nm laser excitation of solution mixtures containing (**b**) [RuPS] = 1 mM, [TEA] = 1 M, [**1**] = 10 mM; and (**c**) [FePS] = 1 mM, [DMA] = 1 M, [**1**] = 10 mM.

These assignments were substantiated by the fact that rates measured in 1) and 3) were first-order in [**1**] while the rate constants measured for 2) were concentration independent suggestive of an intramolecular chemical step. A second-order rate constant of 1.5 x 10^8 M^{-1} s^{-1} was obtained for electron transfer from the monoreduced RuPS to **1**, with the intramolecular cyclization step occurring with a rate constant of 1.5 x 10^5 s^{-1}. The final step that produces **3** is slow with bromine atom transfer from 1 to 4$^{\bullet}$ occurring at a rate constant of 3.6 x 10^6 M^{-1} s^{-1}.

Kinetic analysis conducted with the FePS photocatalysis showed monophasic behaviour that was first-order in [**1**] with a second-order rate constant of 2.3 x 10^8 M^{-1} s^{-1} obtained for electron transfer from FePS^{-} to **1**.

TRIR experiments were not explored for IrPS due to the unavailability of pulsed blue light excitation necessary to excite IrPS. Based on fact that the quenching rate constants for RuPS and IrPS were of the same order of magnitude and that the products distribution and yields were very similar, it seems plausible that both photosensitizers follow the same reaction mechanism. Steady-state PL measurements, as well as transient absorption spectroscopy suggested that excitation of either RuPS or IrPS resulted in electron transfer from TEA to generate the reactive singly reduced photosensitizer and the corresponding TEA$^{\bullet+}$. Electron transfer from these monoreduced photosensitizers to the substrate **1** causes the heterolytic C–Br bond breaking and the subsequent steps the lead to the formation of **3** and **4**.

All the measurements indicate that the initial transformation of **1** is to the dehalogenated radical intermediate **2**$^{\bullet}$, a common mechanistic step for all photosensitizers studied here. This common denominator naturally sparks an intriguing question – *why is the chemoselectivity for product distribution different when FePS drives the catalytic reaction?* Even though cyclization of **2**$^{\bullet}$ to produce **4** is an intramolecular chemical step, it occurs on an early microsecond time scales that allows time for other competitive reaction pathways. We speculate that the conversion of **2**$^{\bullet}$ to **2** requires a H-atom transfer, presumably from TEA$^{\bullet+}$, prior to cyclization. As such, the rate for H-atom transfer is strongly dependent on [TEA$^{\bullet+}$] generated under steady-state illumination conditions. Although the reduction potential of FePS^{-} is about 0.6 V more positive than RuPS^{-} and IrPS^{-}, clearly indicating a significant difference in free energy for electron transfer to **1**, the rate constants for this step were within experimental error the same, ~1.5 x 10^8 M^{-1} s^{-1}. Given that quenching of FePS* by TEA is 2–3 orders of magnitude faster than for RuPS* and IrPS*, a much higher steady-state concentration of TEA$^{\bullet+}$ is present that might favour H-atom transfer over the slow cyclization step.

Taken altogether, the data presented herein allow a plausible mechanism to be proposed for the three photosensitizers (**Figure 10**). Light excitation of the PS yields an excited state that is reductively quenched by triethylamine, [**PS***,TEA] → [**PS**$^{-}$,TEA$^{\bullet+}$]. For RuPS, the cage escape yield ϕ_{CE} was between 0.15 and 0.58, while considerably lower values (0.09-

0.21) were obtained for FePS. The reduced photosensitizer transferred an electron to **1**, which induced heterolytic C–Br bond breaking to yield the **2•** radical. B3LYP and MP2 calculations both confirmed that the LUMO of **1** was centered on the C–Br and ester fragments. Further, the atomic vectors generated from nuclear Fukui functions showed that the C–Br bond exhibited the strongest projected force response along its axis, in line with the observed bond breaking dehalogenation.

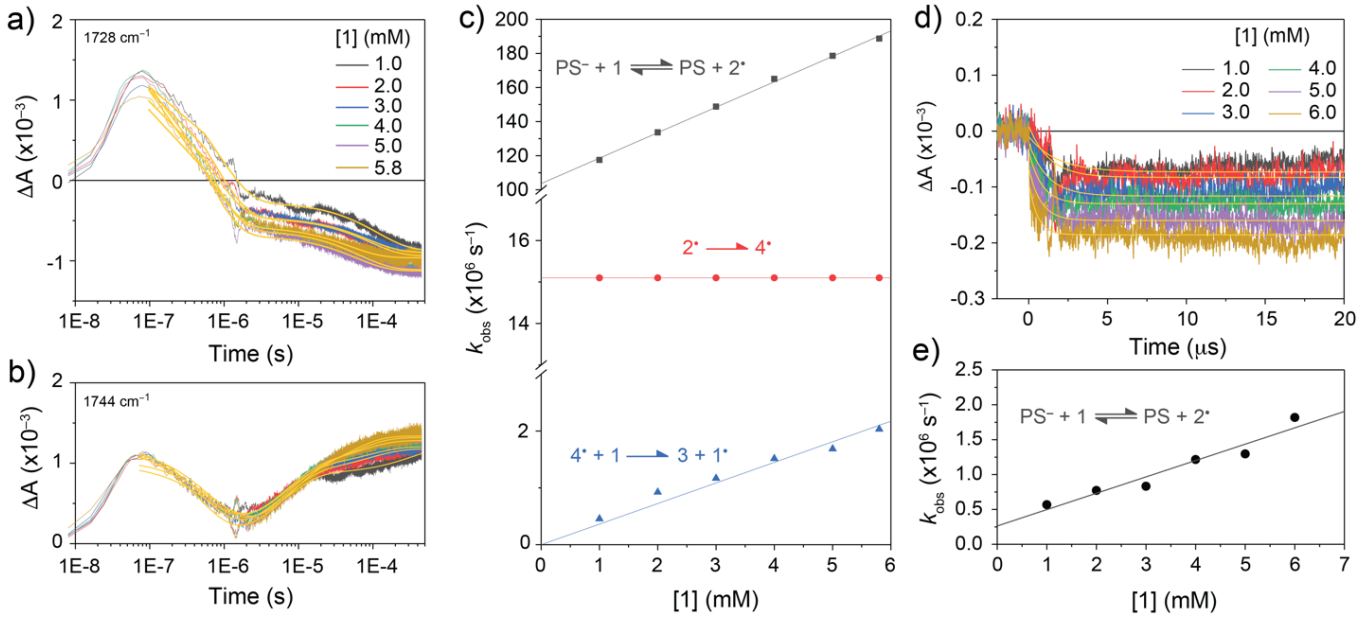

Figure 9. Absorption changes following pulsed 532 nm excitation of RuPS monitored at a) 1728 cm^{-1} and b) 1744 cm^{-1} with the indicated concentration of [**1**] in CH_2Cl_2. c) Pseudo-first-order observed rate constants rates extracted from data in a) and b) plotted against [**1**]; the corresponding reaction chemistries are indicated for each dataset. d) Absorption changes measured at 1728 cm^{-1} for FePS following pulsed 532 nm laser excitation at the indicated [**1**]. e) Pseudo-first-order observed rate constants rates extracted from data in d) plotted against [**1**].

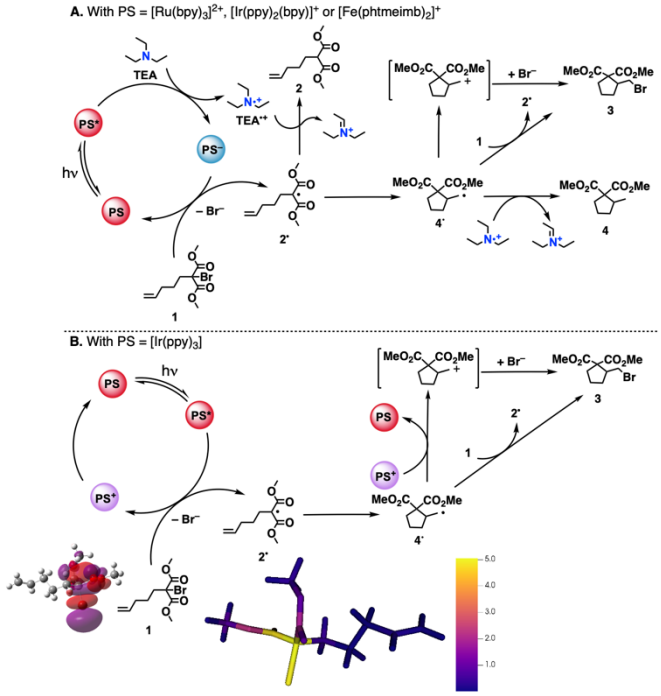

Figure 10. Proposed mechanism for the visible-light mediated dehalogenation of **1**. The LUMO of **1** was calculated at the MP2 level using the 6-311G(g) basis. The magnitude of the nuclear Fukui functions (in a.u.) (B3LYP/6-311G(d)) characterizing the changes in the force that the atoms experience following the electron-attachment in **1** are represented on the lower left.

In the case of RuPS and IrPS, the product distribution is consistent with a pathway where intramolecular cyclisation follows the bond breaking event leading to the cyclical radical **4•**. At this stage, a few pathways are worth considering. First, **4•** abstracts a H-atom from $TEA^{•+}$ to generate **4** as the final product. Second, **4•** reacts with **1** to initiate a propagation reaction that produces **2•** and **4**. Third, **4•** undergoes oxidation (in the dark or under illumination) to generate the putative carbocation that would accept a Br^- to form the corresponding halogenated product **3**. The second proposed pathway is consistent with TRIR observations wherein the slow first-order dependence on [**1**] was assigned to the **4•** + **1** → **3** + **1•** reaction. The product distribution monitored over time during the photoredox reaction showed that **3** was produced with larger reaction rates during the first hour of illumination but quickly reached a plateau, while **4** was formed with a much smaller rate during the 4 hours duration of the experiment. Evidence for the third proposed pathway was obtained for a solution mixture containing $[Ir(ppy)_3]$ in DMF with added LiBr, but in the absence of TEA. Under this condition, the cyclic product **3** was exclusively formed (see experimental section). Stern-Volmer experiments indicated that $[Ir(ppy)_3]^*$ was dynamically quenched by **1** (**Figure S4**) presumably creating the mono-oxidized iridium photosensitizer, $[Ir(ppy)_3]^+$, and reduced **2•**. After intramolecular cyclisation, **4•** is oxidized to the corresponding carbocation to regenerate the $[Ir(ppy)_3]$. The transient carbocation then reacted with LiBr to generate **3** in high yields.

Although speculative, the presence of the non-cyclised product **2** for FePS* may result from a higher steady state concentration of $TEA^{\bullet+}$ that enable PCET to compete kinetically with cyclisation.

Conclusions

The excited state reactivity of three photosensitizers, including two prototypical ruthenium(II) and iridium(III) photosensitizers and one iron(III) photosensitizers was investigated in CH_2Cl_2, CH_3CN and DMF. All photosensitizers were capable of inducing a visible light mediated dehalogenation/cyclization in agreement with C. Stephenson *et al.*.[45] With Ir(III) and Ru(II) photosensitizers, the reaction proceeded with high yields and led to a mixture of cyclized products **3** and **4**. When an Fe(III) photosensitizer was used, the reaction only proceeded quantitatively in CH_2Cl_2 and yielded a mixture of products **2**, **3** and **4** where **2** is non-cyclized. The bottleneck for the efficient use of Fe(III) photosensitizers is the cage escape yield within the encounter complex following excited-state electron transfer. Cage-escape yields were low in polar solvents but reached values of 0.21 with TEA in CH_2Cl_2. As speculated previously, this most probably originates from a combination of increased state-mixing due to the heavy-atom effect, and electrostatic repulsion between the reduced iron photosensitizer and the oxidized electron donor.[44] Mechanistically, time-resolved spectroscopy agreed in all reactions with formation of a monoreduced photosensitizer that then transferred an electron to the halogenated substrate. In agreement with DFT calculation, this electron transfer led to C-Br bond scission, generating an active radical. The mechanism by which this radical continues to react to form the final products remains speculative and will be further studied in the future. Overall, the collective experimental and theoretical data of this study points towards directions that will further advance the development of non-noble transition metal photosensitizers competent of catalyzing reactions important for environmental and energy applications.

Bibliography

Figure 11. Ludovic Troian-Gautier (left) and Renato N. Sampaio (right)

Ludovic Troian-Gautier received his B.Sc. (2008), M.Sc (2010), and Ph.D. in chemistry (2014) from the Université libre de Bruxelles (ULB) under the supervision of Prof. C. Moucheron and Prof. A. Kirsch-De Mesmaeker. He then worked at a spin-off (2014-2015) with Prof. I. Jabin and Dr. A. Mattiuzzi, where he worked on surface modification using calix[4]arene derivatives. Between 2015 and 2019, he performed research within the Alliance for Molecular PhotoElectrode Design for Solar Fuels (AMPED EFRC) directed by Prof. G. J. Meyer at the University of North Carolina at Chapel Hill. In May 2019, he started a *Chargé de Recherches* position (FNRS) at ULB where he worked on energy related challenges. As of October 2021, he continues his research endeavor on energy related challenges as *Collaborateur Scientifique* at the Université Catholique de Louvain (UCLouvain).

Renato N. Sampaio received his B.Sc. (2008), M.Sc (2010), and Ph.D. in Physics (2014) from the Universidade Federal de Uberlândia under the supervision of Prof. N. M. Barbosa Neto. He undertook postdoctoral research (2015-2018) within the Alliance for Molecular PhotoElectrode Design for Solar Fuels (AMPED EFRC) directed by Prof. G. J. Meyer at the University of North Carolina at Chapel Hill. Between 2018 and 2021 he was a research associate at Brookhaven National Laboratory in the Artificial Photosynthesis group directed by Dr. E. Fujita. In July 2021, he accepted a Senior Research Scientist position in the Center for Hybrid Approaches in Solar Energy to Liquid Fuels (CHASE) at the University of North Carolina at Chapel Hill.

Conflicts of interest

There are no conflicts to declare.

Acknowledgements

This work was carried out at the Université catholique de Louvain, the University of North Carolina at Chapel Hill, the Friedrich-Alexander-Universität Erlangen-Nürnberg, Brookhaven National Laboratory and the Université libre de Bruxelles. The Fonds National pour la Recherche Scientifique (F.R.S.-FNRS) is greatly acknowledged for an individual FRIA fellowship (A.A.), the Chargé de Recherches and Collaborateur Scientifique individual fellowship (L.T.-G.) and continuous support (B.E.) as well as the UCLouvain (S.D.K, M.L.S. and B.E.) for support of the iron(III), Ir(III) and Ru(III) photocatalyzed mechanistic studies. R.E.B., J.C.D., R.N.S and G.J.M. acknowledge the Center for Hybrid Approaches in Solar Energy to Liquid Fuels, CHASE, an Energy Innovation Hub funded by the US Department of Energy, Office of Basic Energy Sciences, Office of Science, under award number DE-SC0021173, for support of the nanosecond transient absorption studies. REB acknowledges the National Science Foundation for an individual Graduate Research Fellowship under Grant No. DGE-1650116 for support of the cage-escape yields measurements. Computational resources were provided by the Shared ICT Services Centre, Université libre de Bruxelles. A.C. acknowledges the Argentinian Logistic Network and Dirk M.

Guldi for providing access to transient absorption spectroscopy facilities. The authors acknowledge the Engineering of Molecular NanoSystems (EMNS) for granting access to the Fluorolog instrument. Time-resolved Infrared experiments were performed (R.N.S.) in the laboratories of the Artificial Photosynthesis group at Brookhaven National Laboratory supported by the U.S. Department of Energy, Office of Science, Office of Basic Energy Sciences, Division of Chemical Sciences, Geosciences & Biosciences under contract no. DE-SC0012704.

Notes and references[1]

1. J. K. McCusker, *Science*, 2019, **363**, 484-488.
2. O. S. Wenger, *Chem-Eur. J.*, 2019, **25**, 6043-6052.
3. O. S. Wenger, *J. Am. Chem. Soc.*, 2018, **140**, 13522-13533.
4. D. G. Cuttell, S.-M. Kuang, P. E. Fanwick, D. R. McMillin and R. A. Walton, *J. Am. Chem. Soc.*, 2002, **124**, 6-7.
5. N. Armaroli, *Chem. Soc. Rev.*, 2001, **30**, 113-124.
6. P. Herr, F. Glaser, L. A. Büldt, C. B. Larsen and O. S. Wenger, *J. Am. Chem. Soc.*, 2019, **141**, 14394-14402.
7. O. S. Wenger, *Chem-Eur. J.*, 2021, **27**, 2270-2278.
8. S. I. Ting, S. Garakyaraghi, C. M. Taliaferro, B. J. Shields, G. D. Scholes, F. N. Castellano and A. G. Doyle, *J. Am. Chem. Soc.*, 2020, **142**, 5800-5810.
9. T. Liu, R. Tyburski, S. Wang, R. Fernández-Terán, S. Ott and L. Hammarström, *J. Am. Chem. Soc.*, 2019, **141**, 17245-17259.
10. T. Liu, M. Guo, A. Orthaber, R. Lomoth, M. Lundberg, S. Ott and L. Hammarström, *Nature Chem.*, 2018, **10**, 881-887.
11. Y. Zhang, T. S. Lee, J. M. Favale, D. C. Leary, J. L. Petersen, G. D. Scholes, F. N. Castellano and C. Milsmann, *Nature Chem.*, 2020, **12**, 345-352.
12. Y. Zhang, J. L. Petersen and C. Milsmann, *J. Am. Chem. Soc.*, 2016, **138**, 13115-13118.
13. S. Otto, M. Grabolle, C. Förster, C. Kreitner, U. Resch-Genger and K. Heinze, *Angew. Chem. Int. Ed.*, 2015, **54**, 11572-11576.
14. S. Otto, J. P. Harris, K. Heinze and C. Reber, *Angew. Chem. Int. Ed.*, 2018, **57**, 11069-11073.
15. L. A. Büldt, X. Guo, R. Vogel, A. Prescimone and O. S. Wenger, *J. Am. Chem. Soc.*, 2017, **139**, 985-992.
16. A. K. Pal, C. F. Li, G. S. Hanan and E. Zysman-Colman, *Angew. Chem. Int. Ed.*, 2018, **57,**, 8027−8031.
17. P. Herr, C. Kerzig, C. B. Larsen, D. Häussinger and O. S. Wenger, *Nature Chem.*, 2021, DOI: 10.1038/s41557-021-00744-9.
18. M. D. Woodhouse and J. K. McCusker, *J. Am. Chem. Soc.*, 2020, **142**, 16229-16233.
19. R. H. Temperton, N. W. Rosemann, M. Guo, N. Johansson, L. A. Fredin, O. Prakash, K. Wärnmark, K. Handrup, J. Uhlig, J. Schnadt and P. Persson, *J. Phys. Chem. A*, 2020, **124**, 1603-1609.
20. H. Tatsuno, K. S. Kjær, K. Kunnus, T. C. B. Harlang, C. Timm, M. Guo, P. Chàbera, L. A. Fredin, R. W. Hartsock, M. E. Reinhard, S. Koroidov, L. Li, A. A. Cordones, O. Gordivska, O. Prakash, Y. Liu, M. G. Laursen, E. Biasin, F. B. Hansen, P. Vester, M. Christensen, K. Haldrup, Z. Németh, D. Sárosiné Szemes, É. Bajnóczi, G. Vankó, T. B. Van Driel, R. Alonso-Mori, J. M. Glownia, S. Nelson, M. Sikorski, H. T. Lemke, D. Sokaras, S. E. Canton, A. O. Dohn, K. B. Møller, M. M. Nielsen, K. J. Gaffney, K. Wärnmark, V. Sundström, P. Persson and J. Uhlig, *Angew. Chem. Int. Ed.*, 2020, **59**, 364-372.
21. N. W. Rosemann, P. Chábera, O. Prakash, S. Kaufhold, K. Wärnmark, A. Yartsev and P. Persson, *J. Am. Chem. Soc.*, 2020, **142**, 8565-8569.
22. O. Prakash, P. Chábera, N. W. Rosemann, P. Huang, L. Häggström, T. Ericsson, D. Strand, P. Persson, J. Bendix, R. Lomoth and K. Wärnmark, *Chem-Eur. J.*, 2020, **26**, 12728-12732.
23. B. C. Paulus, S. L. Adelman, Lindsey L. Jamula and James K. McCusker, *Nature*, 2020, **582**, 214-218.
24. Y. Liu, K. S. Kjær, L. A. Fredin, P. Chábera, T. Harlang, S. E. Canton, S. Lidin, J. Zhang, R. Lomoth, K.-E. Bergquist, P. Persson, K. Wärnmark and V. Sundström, *Chem-Eur. J.*, 2015, **21**, 3628-3639.
25. Y. Liu, T. Harlang, S. E. Canton, P. Chábera, K. Suárez-Alcántara, A. Fleckhaus, D. A. Vithanage, E. Göransson, A. Corani, R. Lomoth, V. Sundström and K. Wärnmark, *Chem. Commun.*, 2013, **49**, 6412-6414.
26. L. Lindh, P. Chábera, N. W. Rosemann, J. Uhlig, K. Wärnmark, A. Yartsev, V. Sundström and P. Persson, *Catalysts*, 2020, **10**, 315.
27. K. S. Kjær, N. Kaul, O. Prakash, P. Chábera, N. W. Rosemann, A. Honarfar, O. Gordivska, L. A. Fredin, K.-E. Bergquist, L. Häggström, T. Ericsson, L. Lindh, A. Yartsev, S. Styring, P. Huang, J. Uhlig, J. Bendix, D. Strand, V. Sundström, P. Persson, R. Lomoth and K. Wärnmark, *Science*, 2019, **363**, 249-253.
28. Y. Jiang, L. C. Liu, A. Sarracini, K. M. Krawczyk, J. S. Wentzell, C. Lu, R. L. Field, S. F. Matar, W. Gawelda, H. M. Müller-Werkmeister and R. J. D. Miller, *Nature Comm.*, 2020, **11**, 1530.
29. T. Jiang, Y. Bai, P. Zhang, Q. Han, D. B. Mitzi and M. J. Therien, *Proc. Natl. Acad. Sci. USA*, 2020, **117**, 20430-20437.
30. T. C. B. Harlang, Y. Liu, O. Gordivska, L. A. Fredin, C. S. Ponseca, P. Huang, P. Chábera, K. S. Kjaer, H. Mateos, J. Uhlig, R. Lomoth, R. Wallenberg, S. Styring, P. Persson, V. Sundström and K. Wärnmark, *Nature Chem.*, 2015, **7**, 883-889.
31. P. Dierks, A. Päpcke, O. S. Bokareva, B. Altenburger, T. Reuter, K. Heinze, O. Kühn, S. Lochbrunner and M. Bauer, *Inorg. Chem.*, 2020, **59**, 14746-14761.
32. P. Chábera, Y. Liu, O. Prakash, E. Thyrhaug, A. E. Nahhas, A. Honarfar, S. Essén, L. A. Fredin, T. C. B. Harlang, K. S. Kjær, K. Handrup, F. Ericson, H. Tatsuno, K. Morgan, J. Schnadt, L. Häggström, T. Ericsson, A. Sobkowiak, S. Lidin, P. Huang, S. Styring, J. Uhlig, J. Bendix, R. Lomoth, V. Sundström, P. Persson and K. Wärnmark, *Nature*, 2017, **543**, 695-699.
33. J. D. Braun, I. B. Lozada, C. Kolodziej, C. Burda, K. M. E. Newman, J. van Lierop, R. L. Davis and D. E. Herbert, *Nature Chem.*, 2019, **11**, 1144-1150.
34. A. Cannizzo, C. J. Milne, C. Consani, W. Gawelda, C. Bressler, F. van Mourik and M. Chergui, *Coord. Chem. Rev.*, 2010, **254**, 2677-2686.
35. W. Zhang and K. J. Gaffney, *Acc. Chem. Res.*, 2015, **48**, 1140-1148.
36. G. Auböck and M. Chergui, *Nature Chem.*, 2015, **7**, 629-633.
37. L. Liu, T. Duchanois, T. Etienne, A. Monari, M. Beley, X. Assfeld, S. Haacke and P. C. Gros, *Phys. Chem. Chem. Phys.*, 2016, **18**, 12550-12556.

38. P. Chábera, K. S. Kjaer, O. Prakash, A. Honarfar, Y. Liu, L. A. Fredin, T. C. B. Harlang, S. Lidin, J. Uhlig, V. Sundström, R. Lomoth, P. Persson and K. Wärnmark, *J. Phys. Chem. Lett.*, 2018, **9**, 459-463.
39. S. Xia, K. Hu, C. Lei and J. Jin, *Org. Lett.*, 2020, **22**, 1385-1389.
40. S. Li, B. Zhu, R. Lee, B. Qiao and Z. Jiang, *Organic Chemistry Frontiers*, 2018, **5**, 380-385.
41. B. Huang, Y. Li, C. Yang and W. Xia, *Green Chem.*, 2020, **22**, 2804-2809.
42. A. Gualandi, M. Marchini, L. Mengozzi, M. Natali, M. Lucarini, P. Ceroni and P. G. Cozzi, *ACS Catal.*, 2015, **5**, 5927-5931.
43. S. Parisien-Collette, A. C. Hernandez-Perez and S. K. Collins, *Org. Lett.*, 2016, **18**, 4994-4997.
44. A. Aydogan, R. E. Bangle, A. Cadranel, M. D. Turlington, D. T. Conroy, E. Cauët, M. L. Singleton, G. J. Meyer, R. N. Sampaio, B. Elias and L. Troian-Gautier, *J. Am. Chem. Soc.*, 2021, DOI: 10.1021/jacs.1c06081.
45. J. W. Tucker, J. D. Nguyen, J. M. R. Narayanam, S. W. Krabbe and C. R. J. Stephenson, *Chem. Commun.*, 2010, **46**, 4985-4987.
46. T. U. Connell, C. L. Fraser, M. L. Czyz, Z. M. Smith, D. J. Hayne, E. H. Doeven, J. Agugiaro, D. J. D. Wilson, J. L. Adcock, A. D. Scully, D. E. Gómez, N. W. Barnett, A. Polyzos and P. S. Francis, *J. Am. Chem. Soc.*, 2019, **141**, 17646-17658.
47. M.-I. Takeko, T. Masahiro, M. Takayoshi and O. Tomoko, *Chemistry Letters*, 1994, **23**, 2443-2446.
48. C. Lentz, L. Marcélis, L. Troian-Gautier, K. Robeyns, E. Cauët and B. Elias, *J. Photoch. Photobio. A*, 2021, **405**, 112957.
49. S. Aoki, Y. Matsuo, S. Ogura, H. Ohwada, Y. Hisamatsu, S. Moromizato, M. Shiro and M. Kitamura, *Inorg. Chem.*, 2011, **50**, 806-818.
50. J. A. Gurak and K. M. Engle, *ACS Catalysis*, 2018, **8**, 8987-8992.
51. A. P. Forshaw, R. P. Bontchev and J. M. Smith, *Inorg. Chem.*, 2007, **46**, 3792-3794.
52. L. Troian-Gautier, E. E. Beauvilliers, W. B. Swords and G. J. Meyer, *J. Am. Chem. Soc.*, 2016, **138**, 16815-16826.
53. R. Argazzi, C. A. Bignozzi, T. A. Heimer, F. N. Castellano and G. J. Meyer, *Inorg. Chem.*, 1994, **33**, 5741-5749.
54. J. J. Snellenburg, S. Laptenok, R. Seger, K. M. Mullen and I. H. M. van Stokkum, *Journal of Statistical Software*, 2012, **49**.
55. K. M. Mullen and I. H. M. van Stokkum, *Journal of Statistical Software*, 2007, **18**.
56. I. H. M. van Stokkum, D. S. Larsen and R. van Grondelle, *Biochimica et Biophysica Acta (BBA) - Bioenergetics*, 2004, **1657**, 82-104.
57. R. N. Sampaio, D. C. Grills, D. E. Polyansky, D. J. Szalda and E. Fujita, *J. Am. Chem. Soc.*, 2020, **142**, 2413-2428.
58. L. H. Powell, P. H. Docherty, D. G. Hulcoop, P. D. Kemmitt and J. W. Burton, *Chemical Communications*, 2008, DOI: 10.1039/B802473A, 2559-2561.
59. L. Flamigni, A. Barbieri, C. Sabatini, B. Ventura and F. Barigelletti, in *Photochemistry and Photophysics of Coordination Compounds II*, eds. V. Balzani and S. Campagna, Springer Berlin Heidelberg, Berlin, Heidelberg, 2007, DOI: 10.1007/128_2007_131, pp. 143-203.
60. R. Bevernaegie, S. A. M. Wehlin, B. Elias and L. Troian-Gautier, *ChemPhotoChem*, 2021, **5**, 217-234.
61. A. Juris, V. Balzani, F. Barigelletti, S. Campagna, P. Belser and A. von Zelewsky, *Coord. Chem. Rev.*, 1988, **84**, 85-277.
62. F. Barigelletti, A. Juris, V. Balzani, P. Belser and A. Von Zelewsky, *Inorg. Chem.*, 1983, **22**, 3335-3339.
63. L. Troian-Gautier and C. Moucheron, *Molecules*, 2014, **19**, 5028-5087.
64. J. K. White, R. H. Schmehl and C. Turro, *Inorg. Chim. Acta*, 2017, **454**, 7-20.
65. G. Li, M. D. Brady and G. J. Meyer, *J. Am. Chem. Soc.*, 2018, **140**, 5447-5456.
66. A. Soupart, F. Alary, J.-L. Heully, P. I. P. Elliott and I. M. Dixon, *Coord. Chem. Rev.*, 2020, **408**, 213184.
67. E. T. Luis, H. Iranmanesh and J. E. Beves, *Polyhedron*, 2019, **160**, 1-9.
68. S. Cerfontaine, S. A. M. Wehlin, B. Elias and L. Troian-Gautier, *J. Am. Chem. Soc.*, 2020, **142**, 5549-5555.
69. M. Schmallegger and G. Gescheidt, *Monatsh. Chem.*, 2018, **149**, 499-504.
70. J. C. Scaiano, *J. Phys. Chem*, 1981, **85**, 2851-2855.
71. S. Inbar, H. Linschitz and S. G. Cohen, *J. Am. Chem. Soc.*, 1981, **103**, 1048-1054.
72. J. Hu, J. Wang, T. H. Nguyen and N. Zheng, *Beilstein Journal of Organic Chemistry*, 2013, **9**, 1977-2001.
73. C. Devadoss and R. W. Fessenden, *J. Phys. Chem*, 1991, **95**, 7253-7260.